

Unoccupied electronic structure and momentum-dependent scattering dynamics in Pb/Si(557) nanowire arrays

A. Samad Syed,¹ V. Mikšić Trontl,^{1,*} M. Ligges,^{1,†} S. Sakong,^{1,‡} P. Kratzer,¹ D. Lükermann,² P. Zhou,¹ I. Avigo,¹ H. Pfnür,² C. Tegenkamp,² and U. Bovensiepen¹

¹Fakultät für Physik und Zentrum für Nanointegration (CENIDE), Universität Duisburg-Essen, Lotharstrasse 1, 47057 Duisburg, Germany

²Institut für Festkörperphysik, Leibniz-Universität Hannover, Appelstrasse 2, 30167 Hannover, Germany

(Received 11 June 2015; revised manuscript received 20 August 2015; published 1 October 2015)

The unoccupied electronic structure of quasi-one-dimensional reconstructions of Pb atoms on a Si(557) surface is investigated by means of femtosecond time- and angle-resolved two-photon photoemission. Two distinct unoccupied electronic states are observed at $E - E_F = 3.55$ and 3.30 eV, respectively. Density functional theory calculations reveal that these states are spatially located predominantly on the lead wires and that they are energetically degenerated with an energy window of reduced electronic density of states in Si. We further find momentum-averaged lifetimes of 24 and 35 fs of these two states, respectively. The photoemission yield and the population dynamics depend on the electron momentum component perpendicular to the steps of the Si substrate, and the momentum-dependent dynamics cannot be described by means of rate equations. We conclude that momentum- and direction-dependent dephasing of the electronic excitations, likely caused by elastic scattering at the step edges on the vicinal surface, modifies the excited-state population dynamics in this system.

DOI: [10.1103/PhysRevB.92.134301](https://doi.org/10.1103/PhysRevB.92.134301)

PACS number(s): 73.22.-f, 71.15.Mb, 78.47.J-, 73.20.At

I. INTRODUCTION

Experimental analysis of excited, unoccupied electronic states at surfaces experienced a tremendous development during the past two decades due to opportunities offered by nonlinear photoemission spectroscopy. This method profited in particular from the advancement in short-pulse laser sources that have become by now almost routine. Early experiments utilized the peak intensity increase of short-pulse dye lasers over continuous-wave sources to generate photoelectrons by absorption of two photons simultaneously in two-photon photoemission (2PPE) [1]. Application of femtosecond Ti:sapphire lasers continued this evolution and permitted widespread investigation of ultrafast electron dynamics at surfaces by performing time-resolved experiments using pump-probe techniques [1–4] jointly with theoretical developments [5,6]. Recently, the time resolution has been pushed further to the few-femtosecond regime [7] and well into the attosecond regime [8], offering exciting future opportunities to analyze collective electron dynamics directly in the time domain.

Extensive investigations of image potential states [3,4,9,10] and electronic surface resonances induced by alkali-metal adsorption on metal surfaces [11–13] established that the lifetime of excited electrons is typically several ten to hundred femtoseconds if the respective unoccupied surface state occurs within an orientational band gap. The absence of such an orientational band gap and degeneracy with electronic bulk states leads to ultrafast wave-packet propagation into the bulk [13], which is inherently linked to a broadening of the photoemission linewidth limiting its detection by the

surface-sensitive 2PPE technique. Moreover, hot electron dynamics in quantum-well states in metallic overlayers have been investigated [14]. Relaxation times of a few femtoseconds have been reported for layers on metallic substrates [15,16], which increased to above 100 fs for states in a layer degenerate with a band gap of a semiconducting substrate [17]. These differences suggest that elastic scattering into bulk states on the metallic substrates plays a major role in the relaxation times in metallic overlayers on metallic substrates. All these studies show that hot-electron dynamics in two-dimensional metallic systems has been investigated in detail, and the essential elementary processes relevant in ultrafast electron dynamics are known and understood.

On single-crystal surfaces, one-dimensional (1D) structures such as steps, terrace step decoration, and reconstructions can be prepared using established surface-science methods under ultrahigh-vacuum (UHV) conditions [18]. The influence of steps regarding the scattering and relaxation dynamics of image potential states was investigated on vicinal Cu(100) surfaces [19–24]. In addition to step-induced scattering, these surface systems provide an interesting field of study for one-dimensional physics including spin-charge separation and charge-density-wave (CDW) formation leading to metal-insulator transitions. While pump-induced melting of CDWs in layered crystals has been investigated in the time domain using femtosecond optical [25], time- and angle-resolved direct photoemission [26,27], and transmission electron diffraction [28,29] pump-probe methods, the investigation of photoinduced melting of CDWs on 1D surface reconstructions has so far been limited to surface-sensitive electron diffraction [30]. Rügheimer *et al.* have published a first time-resolved 2PPE study of the one-dimensional Si(557)-Au atomic chain system [31]. That work reported three electronic states, which were absent in electronic structure calculations. Biedermann *et al.* studied the occupied and unoccupied electronic structure of the quasi-one-dimensional Si(553)-Au reconstruction, and they identified an unoccupied spin-split silicon step-edge state [32].

*Present address: Institut za fiziku, Bijenicka 46, HR-10000 Zagreb, Croatia.

†manuel.ligges@uni-due.de

‡Present address: Institute of Theoretical Chemistry, Ulm University, 89069 Ulm, Germany.

In this article, we focus on the quasi-one-dimensional surface system Si(557)-Pb, which was previously shown to exhibit one-dimensional electric conductivity below a transition temperature of $T = 78$ K [33,34], while high-resolution angle-resolved photoemission measurements did not show any noticeable temperature dependence of core- and valence-band photoemission spectra [35,36]. Here we employ angle- and time-resolved 2PPE to analyze the unoccupied electronic structure and study the influence of step edges on electron scattering dynamics. Two electronic bands were identified whose dispersion and binding energies agree reasonably well with results obtained by density functional theory (DFT) calculations. We observe momentum-averaged lifetimes of 24 and 35 fs at energies 3.55 and 3.30 eV above the Fermi level that are explained by a position of these states within an energetic region with a strongly reduced electronic density of states of the Si substrate. Furthermore, varying relaxation rates as a function of electron momentum perpendicular to the step edges were identified that cannot be described by simple rate equation models. We rather have to take anisotropic, momentum-dependent dephasing processes, caused by (quasi)elastic scattering, into account.

II. EXPERIMENTAL SETUP

A tunable femtosecond laser system in combination with a UHV chamber including standard surface-science preparation and characterization tools such as low-energy electron diffraction (LEED) was used for femtosecond time- and angle-resolved 2PPE of the quasi-one-dimensional surface reconstruction Si(557)-Pb. Femtosecond laser pulses were generated by a commercial mode-locked Ti:sapphire-based pulsed laser system (Coherent RegA 9040) operating at a repetition rate of 250 kHz and a central wavelength $\lambda = 818$ nm ($\hbar\omega = 1.52$ eV). The system provides 40 fs pulses with average energies of 6 μ J per pulse. We employed frequency conversion of the fundamental laser output through nonlinear optical processes in a commercial optical parametric amplifier system (OPA, Coherent 9450) for bichromatic 2PPE. The fundamental OPA photon energy was tuned to $\hbar\omega_2 = 1.9$ eV (visible, VIS), and part of the beam was subsequently frequency-doubled in a β -barium borate crystal to $\hbar\omega_1 = 3.8$ eV (ultraviolet, UV). Both pulses were p -polarized. Femtosecond temporal resolution was obtained by controlling the time delay Δt between both pulses. Photoelectrons were analyzed with a self-built position-sensitive time-of-flight spectrometer (pTOF), which employs a commercial position-sensitive delay line anode (RoentDek Handels GmbH, Germany) [37]. This instrument acquires four-dimensional data sets, i.e., photoemission intensity as a function of photoelectron kinetic energy and two mutually independent momentum directions k_x and k_y (Fig. 1). The overall spectral, temporal, and momentum resolution was 60 meV, 70 fs, and 2 m\AA^{-1} , respectively. To avoid electric-field-induced acceleration of the laser excited photoelectrons with few eV kinetic energy, the vacuum levels of the sample and the electrically grounded pTOF spectrometer were aligned by applying an accelerating bias voltage of -400 meV. During all measurements, the sample was cooled by liquid nitrogen, and the data were obtained at a temperature of 85 K (above the previously reported phase-transition temperature [33,34]),

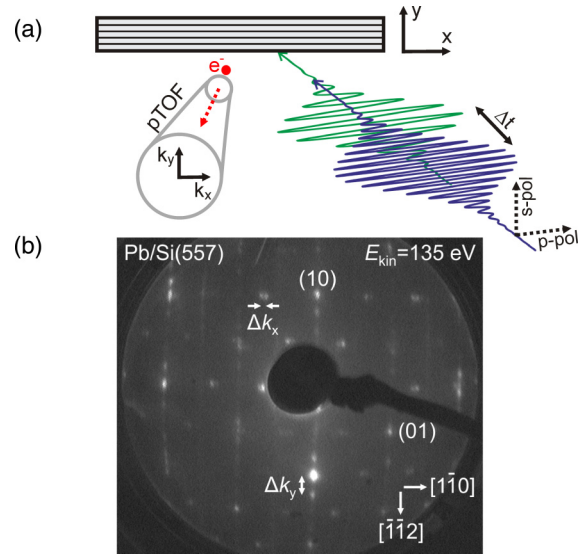


FIG. 1. (Color online) (a) Sketch of the experimental geometry. Unless otherwise specified, both pulses $\hbar\omega_1$ and $\hbar\omega_2$ used for the 2PPE process were p -polarized (parallel to the step edges). Photoemission spectra were recorded by a position-sensitive time-of-flight spectrometer that records photoemission events with momentum components along (k_x) and perpendicular to (k_y) the wire array simultaneously. (b) LEED image from the Si(557)-Pb reconstruction recorded with a primary electron energy of $E_{\text{kin}} = 135$ eV. The high-symmetry directions along ($k_x \parallel [1\bar{1}0]$) and perpendicular to ($k_y \parallel [\bar{1}\bar{1}2]$) the step edges are indicated. The characteristic spot splitting Δk_x and Δk_y is indicative of an equally stepped surface with the proper 1.31 ML Pb coverage [38].

measured by a diode temperature probe mounted adjacent to the Si wafer on the sample holder. During the sample preparation, the temperature was monitored by a calibrated infrared pyrometer (IMPAC IGA 140).

III. SAMPLE PREPARATION AND CHARACTERIZATION

The samples were prepared *in situ* under UHV conditions ($p < 1 \times 10^{-10}$ mbar). Single-crystal Si(557) substrates (p -doped, 1–20 Ω cm, MaTeck Germany) were prepared in a two-step process before Pb deposition. The substrates were first degassed for 10–12 h at 870 K through resistive heating. Subsequently, the samples were trained to maintain UHV conditions at temperatures of 970–1070 K. The native oxide was removed from the sample surface by several flashing cycles at 1320–1370 K. After the last cycle of flashing, the temperature was slowly ramped in the range of 1170–970 K within 5 min to remove surface defects. The morphology of the clean Si(557) sample was verified by LEED.

The nanowire arrays were prepared by Pb deposition onto the clean substrate using a Knudsen cell. The deposition rate (0.5 ML/min) was monitored by a quartz microbalance during the evaporation of a nominal mass flux equivalent to five monolayers (ML) of Pb at 600 K substrate temperature, followed by an additional 3 ML equivalent at 570 K. The deposition at elevated substrate temperature results effectively in a lower surface coverage of 1.31 ML due to a detailed balance between adsorption and desorption. The morphology

of the prepared system was again verified by LEED, as shown in Fig. 1. The observed fourfold spot splitting Δk_y along the $[\bar{1}\bar{1}2]$ direction is indicative of an equally stepped surface with an average step distance of $d_{\text{step}} = 1.59$ nm. The disappearance of the (7×7) reflections from the bare Si substrate goes along with the appearance of new superstructure spots at $\sqrt{3}$ positions, which are split along the $[1\bar{1}0]$ direction, indicating the proper 1.31 ML Pb coverage [38] required for the formation of the Si(557)-Pb nanowire arrays.

The resulting quasi-1D Pb/Si(557) reconstruction consists of Pb-covered terraces with a width of $w_{\text{step}} = 1.55$ nm that are separated by double steps of 0.314 nm height because of a refaceting of the underlying Si(557) surface into a (223) structure. The Pb superstructure is locally composed of a $\sqrt{3} \times \sqrt{3}R30^\circ$ structure, which is regularly interrupted by equally spaced $\sqrt{7} \times \sqrt{3}$ domain walls, yielding an overall tenfold superperiodicity along $[1\bar{1}0]$. For a structural model and further details, see [34].

IV. RESULTS

A. Unoccupied electronic structure

Figure 2 shows the 2PPE data extracted at maximum pump-probe overlap ($\Delta t = 0$) for the two high-symmetry directions along ($k_x \parallel [1\bar{1}0]$) and perpendicular to ($k_y \parallel [\bar{1}\bar{1}2]$) the step direction. Zero in-plane electron momentum refers to normal photoemission from the macroscopic Si(557) surface, which is 9.5° tilted with respect to the microscopic Si(111) terraces. Two distinct intermediate-state signatures A and B can be deduced from the 2PPE signal whose intensity maxima are in normal emission energetically located 3.55(5) and 3.30(5) eV above the Fermi level E_F , respectively. Note that the binding-energy determination is based on an assignment of the populating (UV) and photoemitting (VIS) laser pulses, which is made based on the result of our time-resolved experiments discussed in Sec. IV B. From this population scheme (also sketched in Fig. 2), the states' binding energy with respect to the Fermi level E_F can be calculated as $E - E_F = E_{\text{kin}} + \Phi - \hbar\omega_2$, where the work function $\Phi = 4.35(5)$ eV was determined in a separate direct photoemission experiment using frequency-quadrupled pulses of the fundamental laser wavelength ($4\hbar\omega = 6.06$ eV).

The intensity maxima of both bands, representing $E(k_x, k_y)$, are indicated by the open circles in Fig. 2. Effective electron masses of $m_{x,A}^* = 1.4(2)$ and $m_{y,A}^* = 0.6(1)$ were extracted for the uppermost state A along the high-symmetry directions k_x and k_y . State B shows no simple parabolic dispersion, and we omit a determination of an effective electron mass. The low effective mass of state A perpendicular to the chain direction indicates propagation of the corresponding electron wave function across the steps. This is in contrast to findings for the occupied electronic band structure from earlier direct photoemission work [34], which showed that the Fermi surface of the system consists of anisotropic contours that are replicated with $\Delta k_y = 2\pi/d_{\text{step}}$, and it indicates that electronic excitations far above the electronic band gap of ≈ 20 meV [34] can propagate almost freely above the step edges. On the other hand, the 2PPE yield in the energy window dominated by state A shows a strong dependence of photoemission intensity with k_y (the momentum direction perpendicular to

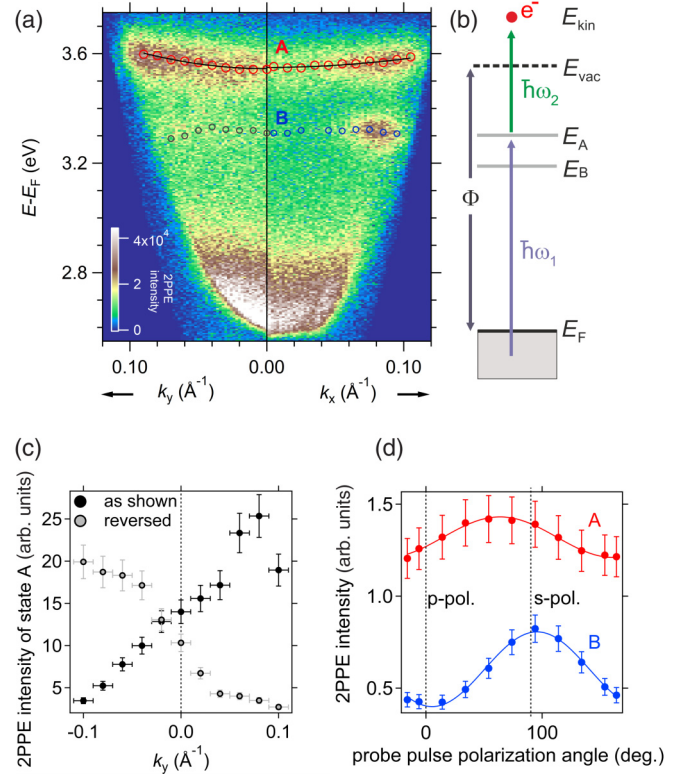


FIG. 2. (Color online) (a) 2PPE spectra recorded parallel (k_x) and perpendicular (k_y) to the wire directions at $\Delta t = 0$ for $\hbar\omega_1 = 3.8$ eV and $\hbar\omega_2 = 1.9$ eV. The energy axis shows the intermediate-state energy, referenced to the Fermi level E_F . Open circles indicate the peak maxima. (b) Schematic energy level diagram for the pump-probe process. Intermediate states with energy E_A and E_B are first populated by the UV pulse ($\hbar\omega_1$). Subsequently, the electrons are promoted above the vacuum level E_{vac} by the VIS pulse ($\hbar\omega_2$), where they are detected with respect to their kinetic energy E_{kin} . (c) Total 2PPE yield (including background) in the energy window dominated by state A as a function of step-perpendicular momentum direction k_y for the dataset discussed throughout the paper (black markers) and for the reversed sample (gray markers). (d) Momentum-averaged 2PPE intensity in the energy window dominated by states A (red markers) and B (blue markers) as a function of probe pulse ($\hbar\omega_2$) polarization.

the step edges), i.e., the state can be well observed for $k_y > 0$, while for $k_y < 0$ the photoemission signal is reduced as shown in Fig. 2 for opposite azimuthal sample orientations. For large negative electron momenta ($k_y \leq -0.06 \text{ \AA}^{-1}$), the photoemission line of signature A starts to broaden, and the underlying incoherent background (that may originate from excitations in the Si substrate) contributes to the overall 2PPE signal in a non-negligible way. Note that throughout the paper, we refer to the overall 2PPE yield (including the background) as the intensity of signature A or B.

The observed momentum dependence of the 2PPE yield cannot be related to the transition matrix elements in 2PPE, as it remains for s , p , and intermediate polarization of both the populating UV and the probing VIS pulse. Furthermore, the effect is inverted when the sample is rotated by 180° around the azimuth angle, providing evidence that the strong contrast in photoemission yield originates from intrinsic properties of the Pb-Si(557) reconstruction. We conclude that this finding

is related to the real-space structure of the reconstruction, where opposite electron momenta k_y correspond to “step-up” and “step-down” situations, respectively. Figure 2 shows furthermore the dependence of the momentum-averaged 2PPE yield for states A and B as a function of the probe pulse ($\hbar\omega_2$) polarization angle. First, only a weak 2PPE intensity contrast of approximately 18% as a function of probe polarization is observed, indicating that the states under investigation do not underlie strict transition selection rules, and thus do not exhibit simple odd- or even- symmetry with respect to the scattering plane [defined by the macroscopic Si(557)-surface]. Secondly, the maximum and minimum photoemission yield is found for s -polarized and p -polarized light only for state B. State A shows a nontrivial dependence on polarization angle. We will catch up on this aspect in Sec. V, where we discuss the origin of states A and B in more detail.

B. Analysis of relaxation dynamics

We will now turn to the ultrafast dynamics observed in the 2PPE experiments, which was obtained by changing the pump-probe delay time Δt between the laser pulses at $\hbar\omega_1$ and $\hbar\omega_2$. Figure 3 shows the 2PPE intensity as a function of Δt after averaging over the accessible momentum space ($|k_x| \leq 0.11 \text{ \AA}^{-1}$, $|k_y| \leq 0.11 \text{ \AA}^{-1}$). A delay-dependent 2PPE intensity can be observed for both intermediate states A and B, as well as for the third, continuum-like signature C, which we did not discuss above. As can be seen in the momentum-resolved 2PPE data (Fig. 2), this spectrally incoherent signature shows no clear k dependence, and thus likely represents secondary electronic excitations. This is also evident from the time-resolved data, where feature C is centered around $E - E_F = 2.7 \text{ eV}$, but it spans over the whole energy range between the secondary edge and the energy range where features A and B are found [3.55(5) and 3.30(5) eV above E_F , respectively].

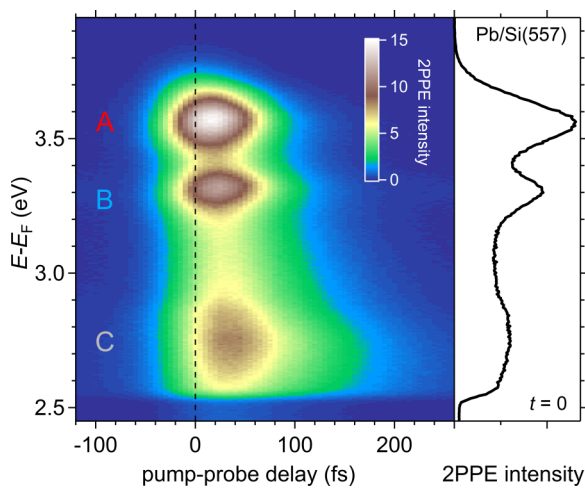


FIG. 3. (Color online) Momentum-averaged 2PPE intensity as a function of pump-probe delay Δt in a false-color representation. Positive delay times refer to the situation in which the intermediate states are populated by the UV pulse ($\hbar\omega_1 = 3.8 \text{ eV}$) and probed by the VIS pulse ($\hbar\omega_2 = 1.9 \text{ eV}$). The right panel shows the momentum-averaged 2PPE spectrum recorded at $\Delta t = 0$.

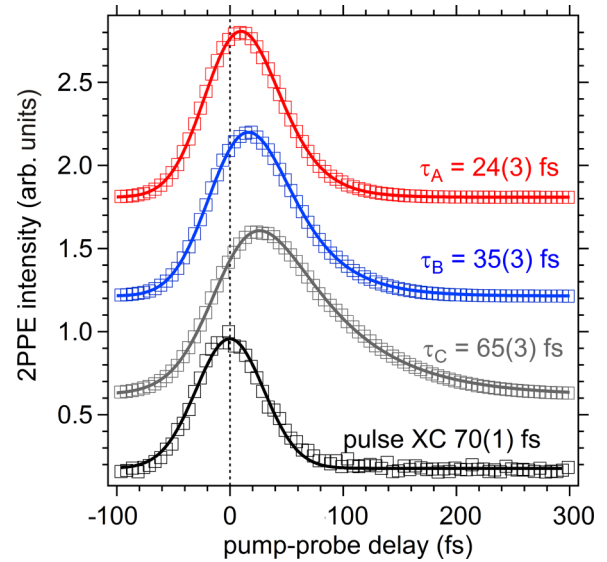


FIG. 4. (Color online) Momentum-averaged population dynamics for the spectral signatures A and B, as well as for the spectrally incoherent continuum signature C. The individual curves are offset for better visibility. The solid lines represent fits based on a rate-equation approach [Eq. (1)]. The pulse cross correlation (XC) was extracted from high-energy carriers in the intermediate-state energy region $E - E_F = 3.73\text{--}3.80 \text{ eV}$.

In general, an energy-dependent relaxation time (indicated by nonsymmetric population dynamics with respect to time zero) can be observed that increases with decreasing energetic distance to the Fermi level. To further quantify the dynamics, we show the 2PPE intensity of all signatures as a function of pump-probe delay in Fig. 4. We deduced the pulse cross correlation (XC) full width at half-maximum from the high-energy carriers (corresponding to intermediate-state energies of $E - E_F = 3.73\text{--}3.80 \text{ eV}$) to be 70(1) fs by fitting a Gaussian function to the population dynamics that shows no clear asymmetry in time, e.g., no resolvable lifetime of the involved electronic states. For all three signatures A, B, and C, a population buildup at negative delay times is observed that subsequently decays toward positive delay times (UV pump, VIS probe). From the temporal evolution of these traces, it is confirmed that these states are originating from intermediate states that are populated by the UV pulses ($\hbar\omega_1 = 3.8 \text{ eV}$) and subsequently photoemitted by the VIS pulses ($\hbar\omega_2 = 1.9 \text{ eV}$). To determine the lifetimes of the states, we use a rate-equation approach:

$$\frac{dN_{\vec{k}}}{dt} = A \exp\left\{-\left(\frac{t}{\sigma}\right)^2\right\} - \frac{\Gamma_{\vec{k}}}{\hbar} N_{\vec{k}}, \quad (1)$$

where $N_{\vec{k}}$ denotes the band's transient population. The first term on the right-hand side accounts for the population buildup due to the pump laser pulse and the finite temporal resolution of the experiment, estimated by a Gaussian of width σ . The second term describes the relaxation with a transition rate $\Gamma_{\vec{k}}$. Such analysis discards intraband scattering processes, as a redistribution of population within the band does not change the momentum-averaged population $N_{\vec{k}}$. Thus, the scattering rate $\Gamma_{\vec{k}}$ can be understood as the inelastic interband scattering

rate that leads to the depopulation of the corresponding band. The analytical solution of Eq. (1), $N_{\vec{k}}(t) \propto \exp\{-\Gamma_{\vec{k}}t/\hbar\}[1 + \text{erf}(t/\sigma - \sigma\Gamma_{\vec{k}}/2\hbar)]$, was fitted to the experimental data under the constraint of the extracted pulse XC width σ . The fit results describe the experimental data very well and are shown in Fig. 4 as solid lines. For the momentum-averaged lifetimes $\tau_{\vec{k}} = \hbar\Gamma_{\vec{k}}^{-1}$ of states A and B, values of $\tau_A = 24(3)$ fs and $\tau_B = 35(3)$ fs were found.

In a next step, we performed a momentum- and time-resolved analysis that allows insight into intraband scattering processes that were discarded in the above momentum-averaged analysis. We focus our discussion on the dynamics observed in the uppermost state A as a function of k_y , because we are interested in step-induced effects that should manifest in symmetry breaking along the in-plane momentum direction perpendicular to the step edges. Here, the most intuitive situation is given when only this momentum direction k_y is considered and $k_x = 0$. Figure 5 shows the population dynamics on a logarithmic intensity scale for the uppermost state A for three different momenta k_y , where k_x was integrated within a window of $\Delta k_x = \pm 0.01 \text{ \AA}^{-1}$ around $k_x = 0$, and windows of width $\Delta k_y = 0.02 \text{ \AA}^{-1}$ were chosen for the analysis. A clear momentum dependence of the population dynamics can be observed that is best visible for positive delay times ($\Delta t > 80$ fs). We observe a momentum-dependent population decay that becomes faster for increasing electron momentum k_y . In contrast to the momentum-averaged analysis, the momentum-dependent population dynamics cannot be described by means of the simple rate-equation approach under the constraint of a fixed pulse cross correlation. In particular,

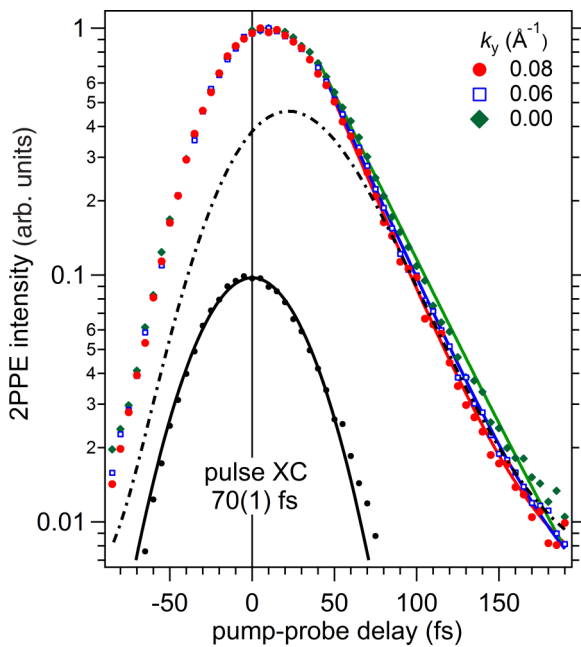


FIG. 5. (Color online) Time-dependent population dynamics for the uppermost state A for selected momentum windows k_y . The dash-dotted line represents a fit based on the rate-equation approach [Eq. (1)], which is insufficiently describing the data. Solid lines represent exponential fits to the trailing edges of the population dynamic traces ($\Delta t \geq 45$ fs).

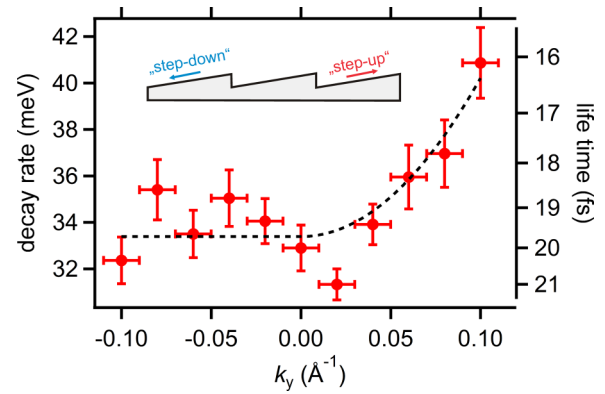


FIG. 6. (Color online) Population decay rates for state A as a function of step-perpendicular in-plane momentum k_y . Error bars along the momentum axis indicate the integration windows used for data analysis. The dashed line is a guide to the eye. The inset sketches “step-down” and “step-up” processes with respect to the macroscopic sample surface.

the time delays of the population maxima, which are known to be an effective measure of the states lifetime [39,40], cannot be reproduced. This is indicated by the dash-dotted line in Fig. 5, which is a least mean-square fit to the population decay observed at positive delay times ($\Delta t \geq 80$ fs) using a fixed pulse XC.

While a more detailed discussion of the complex population buildup at different k_y will follow later in Sec. V, we will first focus on the relaxation dynamics that can be traced by analyzing the population decay at positive delay times. Exponential fits to the trailing edges ($\Delta t \geq 45$ fs) of the population curves, taking into account the temporal resolution of the experiment by convolution with a Gaussian of width σ , are shown as solid lines in Fig. 5. From these fits, changes of the population decay rates $\Gamma(k_y)$ as a function of step-perpendicular in-plane momentum k_y can be observed, and they are summarized in Fig. 6. For $k_y > 0$, the scattering rates gradually increase for larger parallel momentum components k_y . Such a result is expected when intraband scattering processes within a band of effective mass $m^* > 0$ are considered: the primary excited electrons tend to relax toward the band bottom by inelastic scattering, effectively increasing their scattering rate with the states’ energy and, thus, in-plane momentum. Such dynamics was previously observed on isotropic 2D surfaces, e.g., Pb thin films grown on Cu(111) [16], image potential states on a Cu(100) surface [9], and at the Ar/Cu(100) interface [41]. Remarkably, in our case, this decay rate does not change once the band bottom ($k_y = 0$) is passed, since for $k_y < 0$, an almost constant decay rate is observed within the experimental accuracy. This finding goes along with the reduction in photoemission intensity for $k_y < 0$ (Fig. 2), indicating a symmetry breaking for k_y larger or smaller than zero, e.g., situations in which electrons have a finite momentum component toward (“step-down”) or away from (“step-up”) the steps. We will turn toward a more detailed discussion of the possible origins of these effects in Sec. V and first discuss the character of the observed states by comparing our experimental results to DFT calculations in the next subsection.

C. Density-functional-theory calculations

The Pb nanowires on Si(557) locally resemble the structure of a close-packed 2D layer of Pb atoms. This local arrangement is equivalent to the $\sqrt{3} \times \sqrt{3}R30^\circ$ reconstruction with a Pb coverage of 4/3 ML. To support the interpretation of the 2PPE spectra, we therefore performed DFT calculation of a Si(111) slab covered with 4/3 ML Pb in the above reconstruction. The details of the calculation were similar to our previous work [42]. The starting geometry corresponded to the T4 structural model in Ref. [43], and it was reoptimized using the forces calculated from our DFT calculations performed with the VASP code [44]. The electronic exchange and correlation effects were described using the generalized gradient approximation (GGA-PBE) functional [45] and a plane-wave expansion of the wave functions up to a 300 eV cutoff. The Si(111) slab consisted of five bilayers and a hydrogen-passivated backside, and for the lateral supercell dimensions the Si lattice constant of 5.46 Å obtained in PBE was used. The results for the unoccupied Kohn-Sham band structure along the high-symmetry line $\bar{\Gamma}$ - \bar{K} ($\parallel [\bar{1}\bar{1}2]$ or k_y) of the $\sqrt{3} \times \sqrt{3}$ surface Brillouin zone are shown in Fig. 7. We find a considerable spectral weight of Pb-dominated states in the regions $E - E_F = 3.7$ –3.9 and 4.2–4.4 eV above the Fermi energy in the vicinity of the $\bar{\Gamma}$ point. As can be seen from the gray-shaded background of Fig. 7, these Pb-derived bands are found in a spectral region with a strongly reduced electronic density of states in the Si substrate, which is reminiscent of the orientation band gap of single-crystal surfaces of the coinage metals, such as Cu(111). The energetic location of Pb-derived states in this spectral regions results in a weak coupling to the substrate, and it suggests that these states may be long-lived. In particular, the experimentally observed bands A and B can be explained by Pb-derived states in the 3.7–3.9 eV region, with the uppermost band displaying a similar dispersion as the experimental state A. The quantitative differences between the calculated and the measured energy positions could be due to

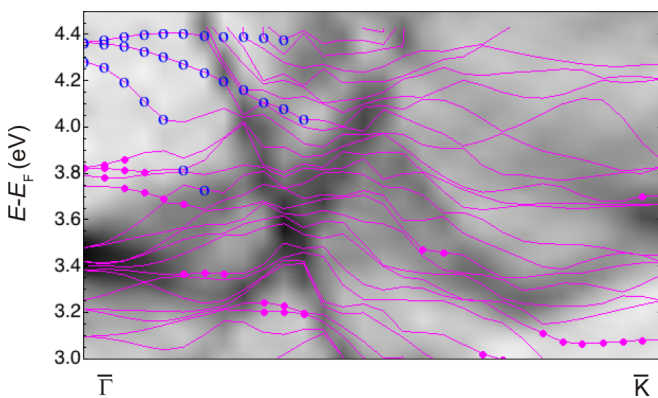


FIG. 7. (Color online) Unoccupied band structure of the $\sqrt{3} \times \sqrt{3}R30^\circ$ Pb/Si(111) reconstruction at 4/3 ML Pb coverage obtained from GGA-PBE calculations. Regions where the projected density of states indicates significant overlap of the Bloch states with Pb $6p_{x,y}$ or $6p_z$ orbitals are highlighted by the open and filled circles, respectively. The gray-scale plot in the background indicates the electronic density of states of bulk Si, with black indicating high density, as obtained from a separate calculation after projection onto the (111) surface normal.

small differences in the Fermi energy in the p -doped samples and/or to the slab used for the calculation. Moreover, only the local environment of the Pb atoms was represented by the calculations, while the stepped surface morphology of the actual samples was disregarded in the DFT calculation.

V. DISCUSSION

We will first turn toward a discussion of the origin of the electronic states, based on the 2PPE results and the DFT calculations. From the experiments, the states' binding energies with respect to the vacuum level E_{vac} were found to be $E_A - E_{\text{vac}} = -0.80(5)$ eV (for state A at $E - E_F = 3.55$ eV) and $E_B - E_{\text{vac}} = -1.05(5)$ eV (for state B at $E - E_F = 3.30$ eV). Our DFT calculations find two unoccupied electronic states that are derived from Pb orbitals with binding energies similar to those observed experimentally. The calculations furthermore identify a downward dispersion for the lower-lying state B, while the higher-lying state A appears to consist of different branches, one of them exhibiting a positive dispersion near $k = \bar{\Gamma}$. From its binding energy with respect to the vacuum level, the uppermost signature A could in principle be originating from an $n = 1$ image potential state (IPS) located in front of the Pb/Si(557) surface [46,47]. This would be further supported by the free-electron-like effective masses found for this state. However, the experimentally observed difference of 2PPE yield for positive and negative k_y shown in Fig. 2 reflects a real-space anisotropy, and such intensity differences were not reported in previous work on IPS residing on vicinal surfaces [19–23]. Furthermore, the dependence of the 2PPE signal of state A on the probe pulse polarization shown in Fig. 2 clearly excludes an electronic state of even symmetry with respect to the scattering plane. Based on this and the DFT calculations in Sec. IV C, we conclude that signature A is not originating from an IPS. However, the image potential may influence the binding energies and dispersions of states A and B. Such effects can lead to a change in the band structure in Fig. 7 calculated by conventional DFT. Nevertheless, we believe that image potential states should be present at the Pb/Si(557) interface. Following the work of Biedermann *et al.* [32], the binding energy of these states is most likely governed by the dielectric properties of the underlying Si substrate since the Pb adlayer will only exhibit reduced polarizability due to the saturation of Si surface dangling bonds. Under these conditions, the $n = 1$ IPS should be expected at a binding energy $E_{\text{IPS}} - E_{\text{vac}} = -0.59$ eV. Indeed, we observed an additional spectral signature in this energetic region when tuning the excitation photon energy to $\hbar\omega_1 = 3.9$ eV, but we omit a more detailed discussion in the framework of this paper.

The momentum-averaged analysis of the time-dependent 2PPE intensities yields lifetimes of $\tau_A = 24(3)$ fs and $\tau_B = 35(3)$ fs for states A and B, respectively (Fig. 4). The fact that discrete electronic states are experimentally observable and the rather long lifetimes support the results from DFT calculation, where the two states were found to be energetically degenerate with a spectral region of reduced electronic density of states of the underlying Si substrate. It should be stressed that these lifetimes are rather long compared to values obtained from measurements performed on other metallic surfaces, unless

IPS or alkali metals on noble metal surfaces [13] were studied. Kirchmann *et al.* [17] investigated hot-electron lifetimes in monolayer-thick lead films epitaxially grown on a Si(111) surface, and they confirmed that, although this system clearly exhibits a quasi-2D electronic structure, carrier lifetimes are dominated by electron-electron scattering and scale according to Fermi liquid theory, $\tau_{\text{FLT}} \propto n^{5/6}(E - E_{\text{F}})^{-2}$, where the power-law dependence on free-carrier density n represents screening of the effective Coulomb interaction and the number of possible scattering partners, and the dependence on energy E accounts for the possible scattering phase space. Based on their results, electrons 3 eV above E_{F} , which are under discussion here, should exhibit lifetimes shorter than 5 fs. Similar small lifetimes were obtained in other nanoscale systems on different substrates, such as atomic Au wires on Si(557) [31], Bi films on Cu(111) [48], epitaxial Ag films on MgO(100) [49], or Pb quantum-well states on Cu(111) [16].

The scattering rates found in the momentum-resolved analysis of the population dynamics within the energy window dominated by state A (Fig. 6) show an interesting dependence on step-perpendicular momentum k_y . For $k_y > 0$, a gradually increasing scattering rate is found that can be explained by means of intraband scattering contributions within a band of effective mass $m^* > 0$, where the phase space available for intraband scattering increases with the states' binding energy and, thus, in-plane electron momentum. Assuming that the scattering rates can be decomposed by comparing the momentum-averaged value (interband scattering) with those obtained for selected momentum windows using Matthiessen's rule, we obtain $\Gamma_{\text{intra}} = 41 \text{ meV} - \Gamma_{\bar{k}} \approx 14 \text{ meV}$ for the data collected at $k_y = 0.1 \text{ \AA}^{-1}$. Even in this most extreme case, this value is only approximately half the interband scattering rate of $\Gamma_{\bar{k}} \approx 27 \text{ meV}$ found from the momentum-averaged dynamics. The population dynamics is thus dominated by interband-scattering events. In contrast, no clear dependence of scattering rate on electron momentum was observed for $k_y < 0$, and the overall values were found to be smaller than those for $k_y > 0$. This finding contradicts the simple picture of an additional (quasi)elastic intraband scattering channel induced by the presence of the steps that is expected to lead to an increase in the overall scattering probability for electrons with finite momentum toward the step edges. The experimentally observed difference in photoemission yield for positive and negative k_y furthermore indicates that additional processes destroy the spectral coherence of this state for negative k_y . Indeed, for large negative momenta ($k_y \leq -0.06 \text{ \AA}^{-1}$), the 2PPE line of state A broadens, and finally for $k_y \leq -0.09 \text{ \AA}^{-1}$, the spectral signature of state A is almost lost and cannot be disentangled from the spectrally incoherent background. The observed rather constant decay rate for $k_y < 0$ is equal to the value at the band bottom of state A and suggests similar inelastic population decay channels for excitations at $k_y < 0$ and $k_y > 0$. For large negative momenta, the observed population dynamics could reflect excitations in the Si substrate. However, such behavior appears unlikely because earlier studies found that excitations in Si and subsequent transport to the surface occur on much longer time scales (100–1000 fs) than are being discussed here [47]. Furthermore, the nearly constant decay rate is already observed for small negative momenta, where the coherent spectral signature of

state A largely dominates the spectrum. We thus conclude that the excitations leading to the spectral incoherent background only play a minor role in the observed population dynamics.

The fact that the additional scattering processes leading to the reduction of spectral coherence of state A cannot be clearly pinpointed in the time domain by extracting inelastic relaxation rates suggests that the underlying physics are beyond a simple rate-equation-based description of the population dynamics observed in the experiment. Indeed, the dynamics in the individual momentum windows cannot be described by such an approach (Fig. 5). To deliver a more suitable description of the complex population dynamics, we consider coherent excitation dynamics that occurs when the electronic excitation and the laser fields have a well-defined phase relation. Such excitation processes set in under resonant excitation conditions and must be considered as we found a possible initial state at $E - E_{\text{F}} = -0.43(5) \text{ eV}$ in our direct photoemission experiments that would allow for such near-resonant excitation of the uppermost spectral signature A. Figure 8 summarizes our experimental findings on the occupied and unoccupied electronic structure and indicates the near-resonant excitation pathways of states A and B. The relevant initial state at $E - E_{\text{F}} = -0.43 \text{ eV}$ is the Si valence-band maximum, and it was also observed in DFT calculations on the Pb/Si(111) system [42] as well as in experimental studies on Au/Si(557) [31] and Au/Si(553) [32].

The resulting dynamics of such near-resonant excitation processes is described by the Liouville–von Neumann (LVN) equations, whose solution is governed by the pure dephasing times T_2^* (elastic scattering), the lifetimes T_1 of the involved states (inelastic scattering), which is equal to our experimentally determined values $\tau(k_y)$, and the momentum-dependent energy detuning $\Delta E(k_y) = [E_{\text{A}}(k_y) - E_{\text{i}}(k_y)] - \hbar\omega_1$ between the energy difference of the initial and intermediate state $E_{\text{A}} - E_{\text{i}}$ and the populating photon energy $\hbar\omega_1$ [39,50–52]. A possible explanation of the observed momentum-dependent

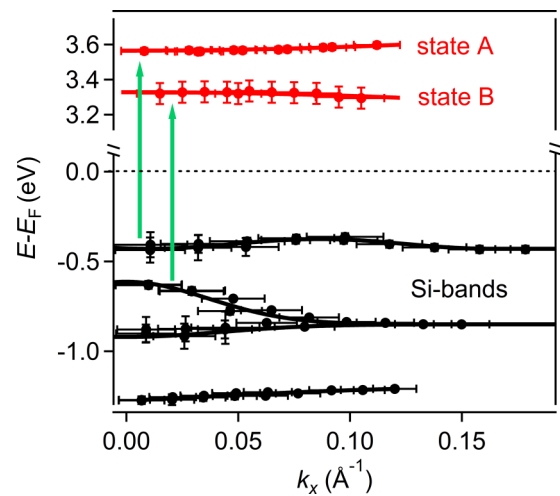


FIG. 8. (Color online) Experimentally determined band structure of the occupied (black) and unoccupied (red) states in the Pb/Si(557) system as a function of in-plane momentum k_x . Error bars along k_x indicate the momentum windows used for the analysis of the binding energy. The near-resonant excitation pathways for states A and B are indicated by the green arrows.

dynamics (see Fig. 6) might be based on the assumption of a strongly anisotropic dephasing time, caused by elastic scattering from the step edges, that changes the population dynamics within individual momentum windows and additionally modulates the total 2PPE yield as a function of k_y [50,53]. A finite dephasing time T_2^* influences both the maximum population of the intermediate state as well as the time of maximum population. In particular, the 2PPE yield is reduced by an increased dephasing rate, as would be expected for step-edge-induced scattering processes, and a population maximum occurring before that given by the rate equation approach can be predicted, as observed experimentally (Fig. 5). However, for a full description of the rich amount of data $I(k_x, k_y, E, t)$ collected in our experiment, intraband scattering has to be explicitly taken into account by coupling the LVN equations for different momentum windows, a task clearly beyond the scope of this paper.

Summarizing, the simple distinction of “step-up” and “step-down” carriers might be oversimplified, but the experimentally observed difference in scattering rates and 2PPE yield for k_y larger and smaller than zero in the most intuitive case of $k_x = 0$ already reflects a non-negligible influence of the local real-space geometry on excited electronic states. The step-induced scattering rate associated with the loss of 2PPE intensity for $k_y < 0$ is considerably larger than those observed in the time domain for image potential states on vicinal Cu(001) [24]. Considering that the scattering at the steps is mediated by the dipolar scattering potential located at step edges [22], such an increase in scattering rate is reasonable due to the larger step-induced dipole at metal-semiconductor hybrid interfaces.

VI. SUMMARY

We observed two unoccupied intermediate states in 2PPE from Pb nanowire arrays grown on a stepped Si(557) surface. Density functional theory calculations find energetically simi-

lar states in the $\sqrt{3} \times \sqrt{3} R30^\circ/\text{Si}(111)$ reconstruction, with the corresponding electronic wave functions being largely located on the lead superstructure. The population dynamics of these states yields lifetimes which suggest that these states are energetically located within a window of reduced electronic density of states of the underlying silicon substrate. Furthermore, momentum-dependent population dynamics was observed that cannot be described within the framework of simple rate equation models. In fact, a pronounced momentum dependence $\Gamma(k_y)$ was found, and it is suggested that a momentum-dependent dephasing rate, possibly caused by elastic scattering from the step edges, is responsible for the nontrivial population dynamics and a difference in 2PPE yield for positive and negative k_y . Our experimental findings are significantly different from those obtained for image potential states on single-crystal vicinal metallic surfaces, indicating that the Pb/Si reconstruction exhibits a stronger dipolar character than metallic surfaces, which finally leads to a strongly anisotropic scattering potential for carriers with finite momentum toward or away from the step edges. Further studies on a possible influence of such anisotropy on scattering dynamics requires a strong theoretical basis to clearly separate intraband scattering processes resulting from energetic relaxation and quasielastic scattering or dephasing processes induced by the presence of the steps.

ACKNOWLEDGMENTS

The authors acknowledge financial support by the Deutsche Forschungsgemeinschaft through FOR1700 “Metallic nanowires on the atomic scale: Electronic and vibrational coupling in real world systems.” V.M.T. is grateful for financial support through the Heinrich Hertz Foundation of the state of Northrhine Westphalia. We furthermore would like to thank Mathias Sandhofer and Ishita Agarwal for experimental support.

-
- [1] T. Fauster and W. Steinmann, in *Electromagnetic Waves: Recent Developments in Research* (Elsevier, Amsterdam, 1995), Vol. 2, p. 347.
 - [2] H. Petek and S. Ogawa, *Prog. Surf. Sci.* **56**, 239 (1997).
 - [3] M. Weinelt, *J. Phys.: Condens. Matter* **14**, R1099 (2002).
 - [4] U. Bovensiepen, H. Petek, and M. Wolf, *Dynamics in Solid States Surfaces and Interfaces, Vol. 1, Current Developments* (Wiley-VCH, Weinheim, 2010).
 - [5] P. M. Echenique, R. Berndt, E. V. Chulkov, T. Fauster, A. Goldmann, and U. Höfer, *Surf. Sci. Rep.* **52**, 219 (2004).
 - [6] R. Knorren, K. H. Bennemann, R. Burgermeister, and M. Aeschlimann, *Phys. Rev. B* **61**, 9427 (2000).
 - [7] X. Cui, C. Wang, A. Argondizzo, S. Garrett-Roe, B. Gumhalter, and H. Petek, *Nat. Phys.* **10**, 505 (2014).
 - [8] S. Neppel, R. Ernstorfer, A. L. Cavalleri, C. Lemmell, G. Wachter, E. Magerl, E. M. Bothschafter, M. Jobst, M. Hofstetter, U. Kleineberg, J. V. Barth, D. Menzel, J. Burgdörfer, P. Feulner, F. Krausz, and R. Kienberger, *Nature (London)* **517**, 342 (2015).
 - [9] W. Berthold, U. Höfer, P. Feulner, E. V. Chulkov, V. M. Silkin, and P. M. Echenique, *Phys. Rev. Lett.* **88**, 056805 (2002).
 - [10] K. Boger, M. Weinelt, and T. Fauster, *Phys. Rev. Lett.* **92**, 126803 (2004).
 - [11] H. Petek, H. Nagano, M. J. Weida, and S. Ogawa, *J. Phys. Chem. B* **105**, 6767 (2001).
 - [12] M. Bauer, S. Pawlik, and M. Aeschlimann, *Phys. Rev. B* **60**, 5016 (1999).
 - [13] J. P. Gauyacq, A. G. Borisov, and M. Bauer, *Prog. Surf. Sci.* **82**, 244 (2007).
 - [14] P. S. Kirchmann and U. Bovensiepen, *Laser Photon. Rev.* **6**, 589 (2012).
 - [15] S. Ogawa, H. Nagano, and H. Petek, *Phys. Rev. Lett.* **88**, 116801 (2002).
 - [16] S. Mathias, A. Ruffing, F. Deicke, M. Wiesenmayer, M. Aeschlimann, and M. Bauer, *Phys. Rev. B* **81**, 155429 (2010).
 - [17] P. S. Kirchmann, L. Rettig, X. Zubizarreta, V. M. Silkin, E. V. Chulkov, and U. Bovensiepen, *Nat. Phys.* **6**, 782 (2010).
 - [18] P. C. Snijders, and H. H. Weitering, *Rev. Mod. Phys.* **82**, 307 (2010).
 - [19] W. Berthold, J. Güdde, P. Feulner, and U. Höfer, *Appl. Phys. B* **73**, 865 (2014).

- [20] T. Fauster, M. Weinelt, and U. Höfer, *Prog. Surf. Sci.* **82**, 224 (2007).
- [21] M. Roth, T. Fauster, and M. Weinelt, *Appl. Phys. A* **88**, 497 (2007).
- [22] M. Roth, M. Weinelt, T. Fauster, P. Wahl, M. A. Schneider, L. Diekhöner, and K. Kern, *Appl. Phys. A* **78**, 155 (2004).
- [23] M. Roth, M. Pickel, M. Weinelt, and T. Fauster, *Appl. Phys. A* **78**, 149 (2004).
- [24] M. Roth, M. Pickel, W. Jinxiong, M. Weinelt, and T. Fauster, *Phys. Rev. Lett.* **88**, 096802 (2002).
- [25] R. V. Yusupov, T. Mertelj, J. H. Chu, I. R. Fisher, and D. Mihailovic, *Phys. Rev. Lett.* **101**, 246402 (2008).
- [26] F. Schmitt, P. S. Kirchmann, U. Bovensiepen, R. G. Moore, L. Rettig, M. Krenz, J. H. Chu, N. Ru, L. Perfetti, D. H. Lu, M. Wolf, I. R. Fisher, and Z. X. Shen, *Science* **321**, 1649 (2008).
- [27] T. Rohwer, S. Hellmann, M. Wiesenmayer, C. Sohr, A. Stange, B. Slomski, A. Carr, Y. Liu, L. Miaja-Avila, M. Kalläne, S. Mathias, L. Kipp, K. Rossnagel, and M. Bauer, *Nature (London)* **471**, 490 (2011).
- [28] M. Eichberger, H. Schäfer, M. Krumova, M. Beyer, J. Demsar, H. Berger, G. Moriena, G. Sciaini, and R. J. D. Miller, *Nature (London)* **468**, 799 (2010).
- [29] T. R. T. Han, Z. Tao, S. D. Mahanti, K. Chang, C. Y. Ruan, C. D. Malliakas, and M. G. Kanatzidis, *Phys. Rev. B* **86**, 075145 (2012).
- [30] S. Wall, B. Krenzer, S. Wippermann, S. Sanna, F. Klasing, A. Hanisch-Blicharski, M. Kammler, W. G. Schmidt, and M. Horn-von Hoegen, *Phys. Rev. Lett.* **109**, 186101 (2012).
- [31] T. K. Rügheimer, T. Fauster, and F. J. Himpsel, *Phys. Rev. B* **75**, 121401(R) (2007).
- [32] K. Biedermann, S. Regensburger, T. H. Fauster, F. J. Himpsel, and S. C. Erwin, *Phys. Rev. B* **85**, 245413 (2012).
- [33] C. Tegenkamp, Z. Kallassy, H. Pfnür, H. L. Günter, V. Zielasek, and M. Henzler, *Phys. Rev. Lett.* **95**, 176804 (2005).
- [34] C. Tegenkamp, T. Ohta, J. L. McChesney, H. Dil, E. Rotenberg, H. Pfnür, and K. Horn, *Phys. Rev. Lett.* **100**, 076802 (2008).
- [35] K. S. Kim, W. H. Choi, and H. W. Yeom, *Phys. Rev. B* **75**, 195324 (2007).
- [36] K. S. Kim, H. Morikawa, W. H. Choi, and H. W. Yeom, *Phys. Rev. Lett.* **99**, 196804 (2007).
- [37] P. S. Kirchmann, L. Rettig, D. Nandi, U. Lipowski, M. Wolf, and U. Bovensiepen, *Appl. Phys. A* **91**, 211 (2008).
- [38] M. Czubanowski, A. Schuster, S. Akbari, H. Pfnür, and C. Tegenkamp, *New J. Phys.* **9**, 338 (2007).
- [39] H. Ueba and B. Gumhalter, *Prog. Surf. Sci.* **82**, 193 (2007).
- [40] T. Hertel, E. Knoesel, M. Wolf, and G. Ertl, *Phys. Rev. Lett.* **76**, 535 (1996).
- [41] M. Rohleder, K. Duncker, W. Berthold, J. Gütde, and U. Höfer, *New J. Phys.* **7**, 103 (2005).
- [42] S. Sakong, P. Kratzer, S. Wall, A. Kalus, and M. Horn-von Hoegen, *Phys. Rev. B* **88**, 115419 (2013).
- [43] T. L. Chan, C. Z. Wang, M. Hupalo, M. C. Tringides, Z. Y. Lu, and K. M. Ho, *Phys. Rev. B* **68**, 045410 (2003).
- [44] G. Kresse, and Furthmüller, *Phys. Rev. B* **54**, 11169 (1996).
- [45] J. P. Perdew, K. Burke, and M. Ernzerhof, *Phys. Rev. Lett.* **77**, 3865 (1996).
- [46] P. M. Echenique and J. B. Pendry, *J. Phys. C* **11**, 2065 (1978).
- [47] P. S. Kirchmann and U. Bovensiepen, *Phys. Rev. B* **78**, 035437 (2008).
- [48] A. Ruffing, S. Vollmar, S. Jakobs, S. Kaltenborn, A. Baral, M. Cinchetti, S. Mathias, H. C. Schneider, and M. Aeschlimann, *Phys. Rev. B* **88**, 075148 (2013).
- [49] M. Aeschlimann, M. Bauer, S. Pawlik, R. Knorren, G. Bouzerar, and K. H. Bennemann, *Appl. Phys. A* **71**, 485 (2000).
- [50] M. Wolf, A. Hotzel, E. Knoesel, and D. Velic, *Phys. Rev. B* **59**, 5926 (1999).
- [51] E. Knoesel, A. Hotzel, and M. Wolf, *J. Electron Spectrosc. Relat. Phenom.* **88-91**, 577 (1998).
- [52] R. Loudon, *The Quantum Theory of Light*, 2nd ed. (Clarendon, Oxford, 1983), p. 39.
- [53] W. L. Chan, J. Tritsch, A. Dolocan, M. Ligges, L. Miaja-Avila, and X. Y. Zhu, *J. Chem. Phys.* **135**, 031101 (2011).